SCIENTIFIC REP⚙RTS

OPEN

Crystal Field Splitting is Limiting the Stability and Strength of Ultra-incompressible Orthorhombic Transition Metal Tetraborides

R. F. Zhang[1,2], X. D. Wen[2,3], D. Legut[4], Z. H. Fu[1], S. Veprek[5], E. Zurek[6] & H. K. Mao[7,8]

The lattice stability and mechanical strengths of the supposedly superhard transition metal tetraborides (TmB_4, Tm = Cr, Mn and Fe) evoked recently much attention from the scientific community due to the potential applications of these materials, as well as because of general scientific interests. In the present study, we show that the surprising stabilization of these compounds from a high symmetry to a low symmetry structure is accomplished by an in-plane rotation of the boron network, which maximizes the in-plane hybridization by crystal field splitting between d orbitals of Tm and p orbitals of B. Studies of mechanical and electronic properties of TmB_4 suggest that these tetraborides cannot be intrinsically superhard. The mechanical instability is facilitated by a unique in-plane or out-of-plane weakening of the three-dimensional covalent bond network of boron along different shear deformation paths. These results shed a novel view on the origin of the stability and strength of orthorhombic TmB_4, highlighting the importance of combinational analysis of a variety of parameters related to plastic deformation of the crystalline materials when attempting to design new ultra-incompressible, and potentially strong and hard solids.

Recently, numerous attempts to design new intrinsically ultraincompressible (bulk modulus $B > 250\,GPa$) and superhard (hardness $H \geq 40\,GPa$) materials evoked much interest in the synthesis of borides of transition metals[1–6] because of their potential applications, such as cutting, drilling, machining and wear-resistant tools with enhanced properties over transition metal carbides[7–9]. In the transition metal borides, a high density of valence electrons of transition metal (Tm) should provide such compounds with high incompressibility, and strong covalent bonds between transition metals and boron should enhance the resistance against plastic deformation. Accordingly, diborides of osmium and rhenium have been synthesized[10,11]. However, although they possess high elastic moduli, the correctly measured load-invariant hardness of ReB_2 and OsB_2 is below 30 GPa. The weak Tm-B and Tm-Tm bonds are responsible for lattice instabilities observed in these diborides[12].

Therefore, much attention turned to the synthesis of triborides or tetraborides of transition metals in which more boron atoms are expected to form a three-dimensional (3D) covalent bond network[1–6]. Using the "hardness models" based on the presumption that large elastic moduli guarantee high hardness, Wang et al.[13] suggested that the 5d transition metal tetraborides, such as WB_4 and MoB_4, should be intrinsically superhard. However, WB_4 synthesized by Gu et al. has load-invariant hardness less than 30 GPa[3], as recently confirmed by Mohammadi et al.[1]. The instability issue raised by Liang et al.[14] and Zhang et al.[15] ruled out the 3D boron network in tetraborides of 5d transition metals. Instead, triborides were proposed to be experimentally accessible because of their thermodynamic, mechanical and dynamic stability, and because of the agreement of the simulated X-ray

[1]School of Materials Science and Engineering, and International Research Institute for Multidisciplinary Science, Beihang University, Beijing 100191, P. R. China. [2]Theoretical division, Los Alamos National Laboratory, Los Alamos, New Mexico 87545, USA. [3]State Key Laboratory of Coal Conversion, Institute of Coal Chemistry, Chinese Academy of Sciences, P.O. Box 165, Taiyuan, Shanxi 030001, P. R. China. [4]IT4Innovations Center, VSB-Technical University of Ostrava, CZ-708 33 Ostrava, Czech Republic. [5]Department of Chemistry, Technical University Munich, Lichtenbergstr. 4, D-85747 Garching, Germany. [6]Department of Chemistry, State University of New York at Buffalo, Buffalo, NY 14260-3000, USA. [7]Geophysical Laboratory, Carnegie Institution of Washington, NW Washington, DC 20015, USA. [8]Center for High Pressure Science and Technology Advanced Research, Shanghai 201203, P.R. China. Correspondence and requests for materials should be addressed to R.F.Z. (email: zrf@buaa.edu.cn)

1

diffraction (XRD) pattern with the experimental one[6]. In recent experiments by Chen et al.[16] and Tao et al.[17], the theoretically proposed structure of WB$_3$ was confirmed experimentally by XRD, high-resolution transmission electron microscopy (HRTEM) and Rietveld refinement. The load-invariant hardness was about 25.5 GPa[17], thus WB$_3$ is not intrinsically superhard. The physical origin of weakening of WB$_3$ lies between the metallic W-B bonds which are responsible for the lattice instability under shear deformation[6], being similar to what has been shown in ReB$_2$[18]. In view of these facts, the majority of recent attempts in the search for new superhard materials focused on transition metal borides with a 3D covalent bond network. After an exploration of several borides, researchers focused their attention on the orthorhombic TmB$_4$ (Tm = Cr, Mn and Fe) in which each Tm atom is surrounded by a 3D covalent boron cage.

Several years ago, the high values of ideal shear strength of >50 GPa and hardness of ~48 GPa theoretically predicted for CrB$_4$ by Niu et al.[19,20], initiated many investigations into this material. However, the synthesized CrB$_4$ has hardness only between 23.3 GPa[21] and 28.6 GPa[22] in agreement with the theoretical calculations by Li et al.[23] Similar discrepancies between theoretical predictions and experimental results were found also for orthorhombic FeB$_4$. Recently, Gou et al.[24] reported a surprisingly high value of hardness for FeB$_4$ of about 67 GPa for a "nanoindentation" depth of 20 to 40 nm. However, it is not clear if this value corresponds to the "asymptotic hardness" as recommended in ref. 25 for correctly measured load-invariant hardness that is obtained under conditions of fully developed plasticity[26]. This high value has been questioned by density functional theory (DFT) calculations of the anisotropic compressibility by Gou et al.[27] and of the ideal strength by Li et al.[28]. More recently, Wang et al.[29] reported a much lower hardness of synthesized FeB$_4$ of 15.4 GPa in agreement with the theoretical calculations.

The question thus arises as to why the 3D covalent network in these tetraborides does not provide the presumed high hardness enhancement. For convenience, we use the nomenclature "Pearson symbol [space group number]" to denote the crystal structures, such as oI10[71] and oP10[58]. Although the oI10[71] structure was proposed for the experimentally synthesized CrB$_4$ and FeB$_4$, it has been latter found to be unstable, and should be substituted by oP10[58] structure[19,27,28,30–33]. The question why the low symmetry oP10[58] structure is energetically favorable and dynamically stable, remained so far unsolved. In order to clarify these questions, we shall study in the present work by means of DFT calculations the following problems: 1) What is the electronic origin of the stabilization from dynamically (phonon) unstable oI10[71] to dynamically stable oP10[58]? 2) What is the upper limit of mechanical strength of oP10[58]-TmB$_4$? 3) Does the bond deformation path and electronic instability mode of TmB$_4$ under shear resemble those of other borides such as ReB$_2$ and WB$_3$? 4) Could the three-dimensional covalent network in TmB$_4$ support a higher plastic resistance?

Results

Stabilization from oI10[71]- to oP10[58]-TmB$_4$. We first searched the most stable structures of stoichiometric TmB$_4$ by geometry optimizations of 26 commonly observed Tm-B, Tm-C, Tm-N, Tm-Al, Tm-Si ICSD structure types[34]. The geometries were optimized using DFT as implemented in the VASP code[35,36]. The details of the adopted initial structures of TmB$_4$ are given in the supplementary materials. The formation energy/enthalpy $\Delta E = \frac{1}{5}[E(TmB_4) - E(Tm) - 4E(B)]$ was calculated from the chemical reaction Tm + 4B = TmB$_4$. The energies of α−B and Tm in magnetic state were adopted as the reference ground states. Figure 1 shows the calculated formation enthalpy of CrB$_4$ and FeB$_4$. The most negative formation enthalpies of oP10[58] indicate that it is the most energetically favored structure. As listed in Table S1 of the supplementary materials, eight typical structures, such as oP10[58], oI10[71], oP10[59], hP20[194], hP10[194], mS10[12], mS20[14] and mS30[12], have been reported for transition metal tetraborides. In the present study, the oP10[58] is found to be the most stable one for both CrB$_4$ and FeB$_4$. The formation enthalpies obtained in the present study for the oI10[71] structure of CrB$_4$ ($\Delta H = -0.301$ eV/atom) and of FeB$_4$ ($\Delta H = -0.143$ eV/atom) are slightly higher than those calculated in previous publications of $\Delta H = -0.3098$ eV/atom for CrB$_4$[37], and of $\Delta H = -0.1698$ eV/atom for FeB$_4$[37]. Note that the initial structure with the mS20[14] symmetry transforms into oP10[58] for both CrB$_4$ and FeB$_4$. Our evolutionary structure search scheme[38,39] confirms further that oP10[58] is the most stable one. A systematic thermodynamic investigation of possible ground state structures with consideration of vibrational entropy has been performed on FeB$_4$ by Kolmogorov et al.[33] Their results indicate that the oP10[58]-FeB$_4$ are thermodynamically stable in the considered temperature range, but it lies 3 meV/atom above the α−B <−> oP12-FeB$_2$ tieline at T = 0 K while 10 meV/atom below the tieline at T = 900 K[33]. The decomposition energy from FeB$_4$ to oP12-FeB$_2$ and α-B are calculated to be positive (~0.01 eV/atom), while the energy from FeB$_4$ to oP8-FeB and α−B are negative (~ −0.02 eV/atom), in agreement with previous calculations[33].

A similar trend of thermodynamic stability is also observed for MnB$_4$ in oI10[71] and oP10[58] structures. The formation enthalpy of oI10[71]-MnB$_4$ of −0.2704 eV/atom decreases slightly by 0.01 eV/atom (0.0097 eV/atom[37]) due to the transformation to the oP10[58] structure whose formation enthalpy is −0.2804 eV/atom. All these calculations suggest that oI10[71]-TmB$_4$ is thermodynamically unstable with respect to oP10[58]-TmB$_4$. Note that a Peierls distortion mechanism has been proposed as the origin of stabilization of mS20[14]-MnB$_4$. However, such distortion will be hindered by temperature and the phonon assisted crossover observed from nonmagnetic Peierls insulator (mS20) to a magnetic Stoner metal (oP10)[30]. Taking CrB$_4$ as a prototype, Fig. 2a,b show the typical bonding feature of oI10[71] and oP10[58]-TmB$_4$. Although the boron network undergoes a significant distortion during the oI10[71] → oP10[58] transformation, the molar volume changes a bit and the simulated XRD figures show a similarity between oI10[71] and oP10[58], but some minor XRD peaks show up for oP10[58] structure which may be identified by experiments[40].

As the next step we calculated the phonon dispersion curves as shown in Fig. 2c,d for CrB$_4$, (Figs S1 and S2 for FeB$_4$ and MnB$_4$). Our phonon calculations suggests that oI10[71] is dynamically unstable for all three tetraborides, while the oP10[58] structure is dynamically stable (see Fig. 2c,d for CrB$_4$). Similar phonon instabilities for oI10[71]-FeB$_4$ and oI10[71]-MnB$_4$ are presented in the supplementary materials as Figs S1 and S2. The phonon

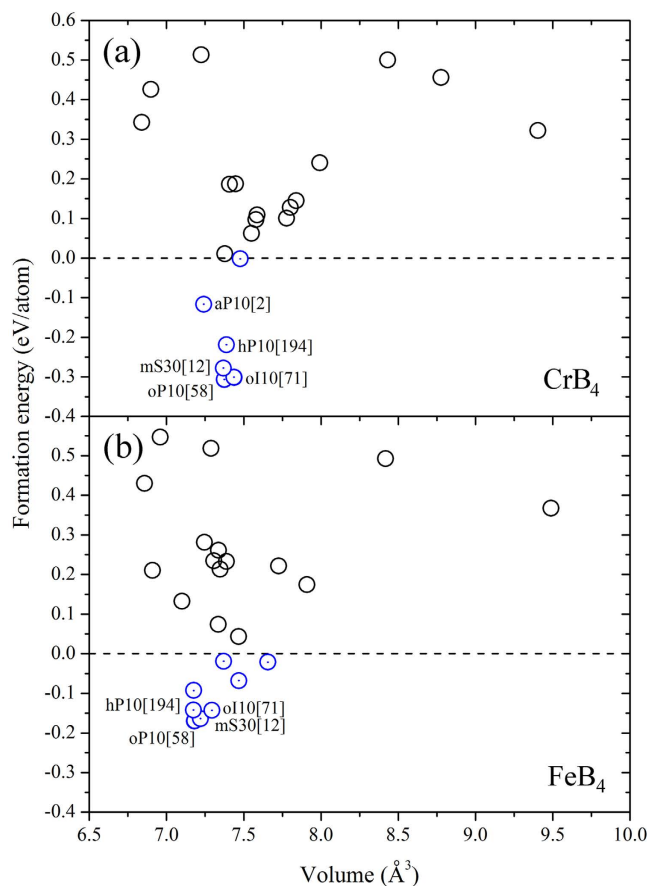**Figure 1. Formation energies of TmB₄ after geometrical optimizations.** Formation energy of (**a**) CrB$_4$ and (**b**) FeB$_4$ calculated by DFT to determine the possible ground state phases of 26 commonly observed Tm-B, Tm-Al, Tm-P, Tm-O, Tm-S ICSD structure types and the newly reported tetraborides. The most stable structure is confirmed by our evolutionary search method.

dispersion relation of $oI10[71]$-TmB$_4$ exhibits at the Γ-point imaginary phonon frequencies, thus showing its dynamic instability at T = 0 K. This result is in agreement with the previous studies of FeB$_4$ by Kolmogorov *et al.*[33] It should be noted that the $oI10[71]$-TmB$_4$ structure comprised of tetragonal boron network has been previously examined within the extended Huckel method. It has been concluded that maximum binding in the 3d series is achieved for Cr, and that the electron-rich Mn, Fe, Co and Ni tetraborides may be unstable in this configuration[41]. Our present results clearly show that the dynamic instability applies for all the three $oI10[71]$-TmB$_4$. In contrast, the $oP10[58]$-CrB$_4$, $oP10[58]$-MnB$_4$ and $oP10[58]$-FeB$_4$ phases are stable as there are no imaginary modes.

With focus on the phonon-assisted transformation from $oI10[71]$ to $oP10[58]$, we attempted to find the electronic origin of the stabilization from higher symmetry structures to those with lower symmetry. After comparing the electronic structure of $oI10[71]$- and $oP10[58]$-CrB$_4$, we found that the transformation from $oI10[71]$ and $oP10[58]$ induces a highly directional electronic partition at two inequivalent sites of the boron atoms in the $oP10[58]$ structure: one with minor charge transfer of ~0.12 electrons, and the other one with a higher charge transfers of ~0.32 electrons. Eight equivalent boron sites are found in $oI10[71]$ structure with an average Bader charge of ~0.22 electrons. The stronger anisotropy of charge transfer in $oP10[58]$ structure indicates its higher electronic polarization and localization as compared to $oI10[71]$ one. The Bader charge density analysis[42] shown in Fig. 2 confirms the different charge transfer at crystallographic sites of Cr for $oI10[71]$ structure (+0.90 electrons) and $oP10[58]$ structure (+0.88 electrons), suggesting a slightly higher ionic contribution for the former. The anisotropy of Bader charges can be attributed to the changes from regular to distorted boron network where metal atoms are donating electrons to stabilize the $oP10[58]$ structure. The analysis of crystal orbital overlap population (COOP) curves of $oI10[71]$- and $oP10[58]$-CrB$_4$ shown in Fig. 2e,f, provides a further confirmation of slightly higher COOP(Cr-B) of 0.28 in $oP10[58]$ structure as compared with $oI10[71]$ structure (0.26). Note that an average COOP value of bonds is used to do the comparison for convenience. Similar higher values of COOP(Fe-B) (0.23) and COOP(Mn-B) (0.20) are also shown for $oP10[58]$ structure as compared to $oI10[71]$ structure (0.21 and 0.18 for Fe-B and Mn-B bonds respectively) (refer to Figs S3 and S4 in supplementary materials). This suggests a slightly stronger bond strength for $oP10[58]$ structure. When observing the structures in Fig. 2a,b one notices much "dense" bond network in $oP10[58]$ structure as compared with $oI10[71]$, which is a qualitative but illustrative confirmation of the analysis of the electronic structure.
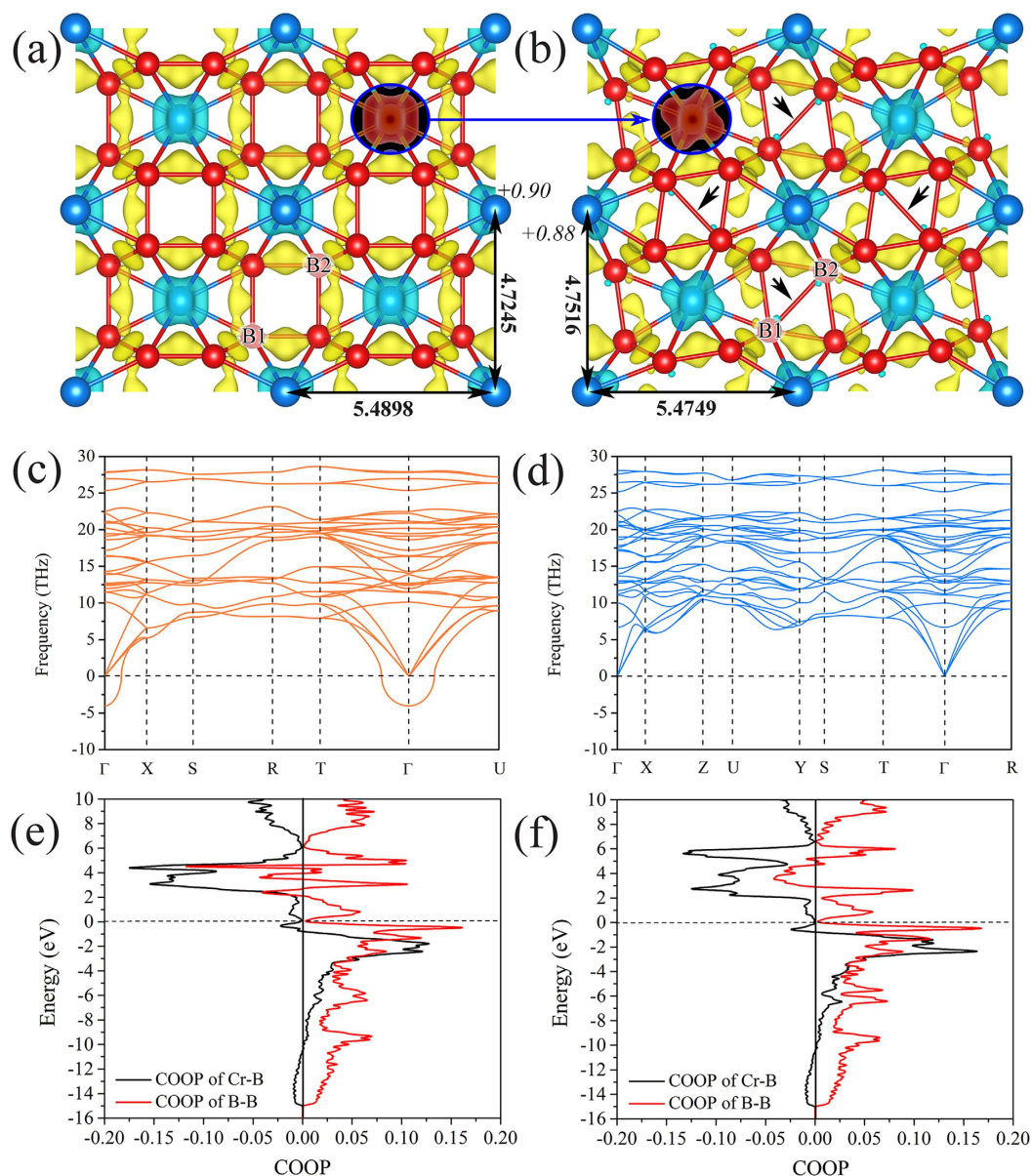
Figure 2. Structure and properties at equilibrium. The equilibrium bond geometry of (**a**) $oI10[71]$- and (**b**) $oP10[58]$-CrB$_4$ viewed along the crystallographic [001] direction, i.e. z axis in Cartesian coordinate system such that the x and y axes are along the crystallographic [100] direction and [010] direction respectively. The isosurfaces maps of the valence charge density difference (VCDD) correspond to $+/-0.01$ electrons/Bohr^3, the large blue and small red spheres represent Cr and B atoms, respectively. Calculated phonon dispersion curves for (**c**) $oI10[71]$- and (**d**) $oP10[58]$-CrB$_4$. The calculated COOP curve for (**e**) $oI10[71]$- and (**f**) $oP10[58]$-CrB$_4$. The numbers close to the Cr atoms in Fig. 1a,b are the corresponding Bader charges. The bold numbers close to the line arrow in (**a,b**) are the neighbor distances between two neighboring Cr-Cr atoms in unit of Angstrom.

The calculated valence charge density difference (VCDD) of $oI10[71]$- and $oP10[58]$-CrB$_4$ shown in Fig. 2 provide additional support of their stabilization by crystal field splitting of the d orbitals. By comparing the isosurface of VCDD of the $oI10[71]$-CrB$_4$ (Fig. 2a) with that of $oP10[58]$-CrB$_4$ (Fig. 2b) we see a big difference in the shape of VCDD isosurface at the metal sites: the VCDD isosurface show anisotropic shape in $oP10[58]$-CrB$_4$, whereas they are relatively isotropic in $oI10[71]$-CrB$_4$. This suggests that although $oP10[58]$ has a lower lattice symmetry, it possess a stronger electronic directionality (see Fig. 2a,b), in agreement with the analysis of charge transfer and COOP analysis in the preceding paragraph. In order to get such electronic partition of d orbitals, the boron network in $oI10[71]$ structure needs to reorganize its positions to transform into $oP10[58]$ structure by rotation operations. Furthermore, the boron-boron bonds indicated by the black arrows in $oP10[58]$ structure (Fig. 2b) are absent in the $oI10[71]$ structure, as seen by the hollow sites in $oI10[71]$ in Fig. 2a.
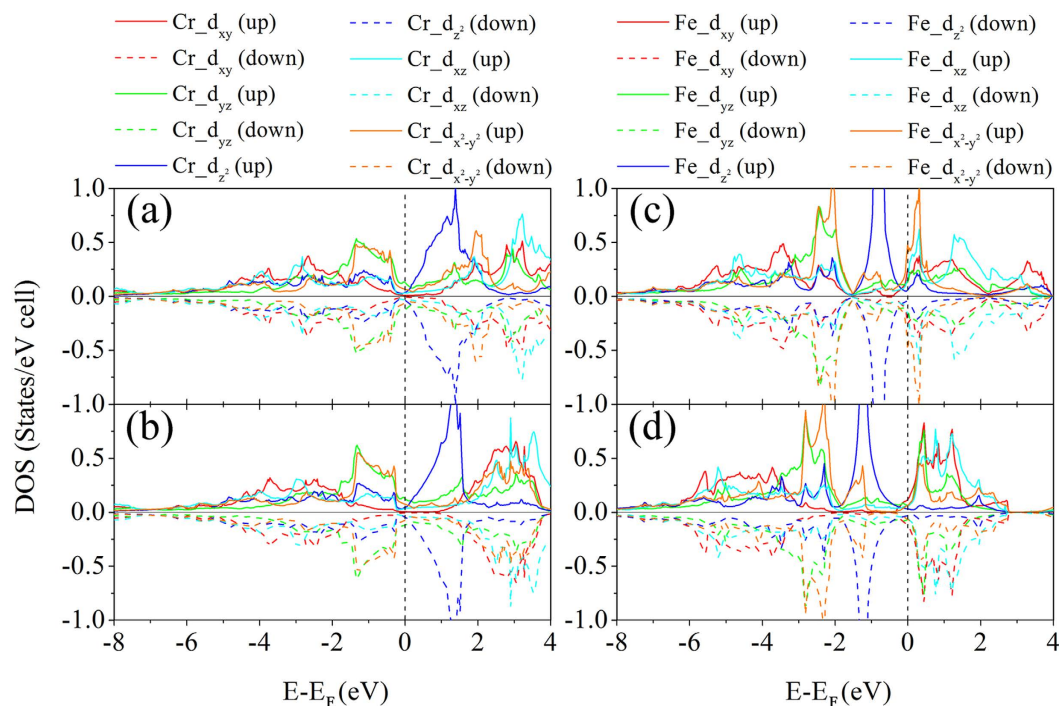
Figure 3. Orbital-decomposed electronic density of states of 5d orbitals of transition metals. (a) $oP10[58]$-CrB$_4$, (**b**) $oI10[71]$-CrB$_4$, (**c**) $oP10[58]$-FeB$_4$ and (**d**) $oI10[71]$-FeB$_4$. The transformation from $oI10[71]$ to $oP10[58]$ corresponds to a change of DOS shape and relative position of the decomposed d orbitals, which is more pronounced for FeB$_4$. The reference Cartesian coordinates was chosen such that the x, y and z axes are along the crystallographic [100] direction, [010] direction and [001] direction respectively. The vertical dashed lines indicate the Fermi levels.

Figure 3 shows the calculated orbital decomposed electronic density of states (DOS) for CrB$_4$ and FeB$_4$ in $oI10[71]$ and $oP10[58]$ structures in their spin polarized states. Figures S5–S7 in the supplemental materials provide additional DOS curves for TmB$_4$. Both structures show metallic bonding because of finite value of DOS at the Fermi level (E_F), which originates mostly from the d-orbitals of Tm and the p-orbitals of B. In the $oI10[71]$-CrB$_4$, the DOS around E_F (0.88 states/eV cell) is slightly higher than that in $oP10[58]$-CrB$_4$ (0.80 states/eV cell), indicating a stronger "splitting" of bonding and antibonding states for $oP10[58]$-CrB$_4$, in agreement with the preceding COOP analysis. A similar feature is observed for MnB$_4$, but does not apply for $oI10[71]$ and $oP10[58]$-FeB$_4$ in which the Fermi level is located at the left shoulder of a peak in the DOS. Such differences will be shown to be responsible for their different shear moduli in the following section. Interestingly, we find in Fig. 3 a distinct change of the majority of $d_{x^2-y^2}$ and d_{xy} orbitals (which mainly contribute to the in-plane rotation) below and above E_F when the structure changes from $oI10[71]$ to $oP10[58]$ for both CrB$_4$ and FeB$_4$, suggesting that crystal field splitting of d orbitals is responsible for the phonon-assisted stabilization from $oI10[71]$ to $oP10[58]$ as discussed above. In case of CrB$_4$, the first peak of $d_{x^2-y^2}$ below the E_F move upward by 0.1 eV during the transformation from $oP10[58]$ to $oI10[71]$, while the first peak of d_{xy} below E_F (at -1.167 eV) nearly disappears. For FeB$_4$ however, the unexpected peaks show up at the Fermi level for $oP10[58]$ structure, but not for $oI10[71]$ structure.

Mechanical properties of $oP10[58]$-TmB$_4$. We next explore the mechanical properties of the $oP10[58]$-TmB$_4$ with Tm changing from Cr to Mn and to Fe. The calculated elastic constants of $oP10[58]$-TmB$_4$ are listed in Table S2 of the supplemental materials and compared with the results from other publications. It is shown that our present calculations are in good agreement with the others, and all the three orthorhombic tetraborides meet the requirements of elastic stability[43] The Voigt average bulk and shear moduli are derived from elastic constants and compared with other hard materials in Table 1[19,23,27,28,31–32,44–48]. It is seen that all three $oP10[58]$ tetraborides are ultra-incompressible materials owing to their high bulk moduli of more than 250 GPa. A relatively high value of shear moduli is observed for $oP10[58]$-CrB$_4$ (267 GPa) and $oP10[58]$-MnB$_4$ (247 GPa), suggesting they are stiff. However, a much lower value found for $oP10[58]$-FeB$_4$ (192 GPa), indicates that it may be less stiff than the other two tetraborides, in agreement with the aforementioned DOS analysis that suggests a stronger metallic bonding for FeB$_4$.

Well established criterion for whether a solid is ductile or brittle is if dislocation embryos can be nucleated from an atomically sharp crack prior to the crack propagation[49,50]. If this is the case at a given temperature, the solid is considered to be intrinsically ductile[49,50]. This distinction of the mechanical behavior is characterized by the ratio of the shear to bulk modulus G/B, based on the consideration that B is a measure of the resistance to fracture and G the resistance to plastic deformation[49,51,52]. The critical G/B ratio which separates ductile and brittle materials is around 0.57, i.e. if $G/B < 0.57$ the material is ductile, and it is brittle when $G/B > 0.57$[51,52]. In view of

Compound	Reference	B_V	G_V	σ_{min}	τ_{min}
CrB$_4$	This study	279	267	$\sigma_{<100>} = 51.0$	$\tau_{(110)[1\bar{1}0]} = 36.2$
	19	265	261	$\sigma_{<100>} = 51$	$\tau_{(010)[101]} = 51$
	23	263	267		$\tau_{(110)[1\bar{1}0]} = 36.7$
	31	237*	255*		
MnB$_4$	This study	281	247	$\sigma_{<101>}49.0$	$\tau_{(110)[001]} = 35.1$
	19	270	245		
FeB$_4$	This study	285	192	$\sigma_{<100>} = 44.0$	$\tau_{(110)[001]} = 25.7$
	19	253	177		
	28	284	194		$\tau_{(110)[001]} = 24.1$
	48	265	198	$\sigma_{<111>} = 40.4$	$\tau_{(111)[11\bar{2}]} = 24.6$
	27	268	189		
	31	250*	181*		
	32	277	186		
WB$_3$	6	293	245	$\sigma_{<10\bar{1}0>} = 43.3$	$\tau_{(0001)[10\bar{1}0]} = 37.7$
MoB$_3$	6	276	226	$\sigma_{<10\bar{1}0>} = 37.7$	$\tau_{(0001)[10\bar{1}0]} = 36.1$
OsB$_2$	44	313	181	$\sigma_{<100>} = 22.5$	$\tau_{(001)[100]} = 9.2$
ReB$_2$	12	348	274	$\sigma_{<\bar{1}2\bar{1}0>} = 58.5$	$\tau_{(0001)[10\bar{1}0]} = 34.4$
B$_6$O	45	231	218	$\sigma_{<10\bar{1}0>} = 53.3$	$\tau_{(0001)[10\bar{1}0]} = 38.0$
BN	46	376	390	$\sigma_{<111>} = 55.3$	$\tau_{(111)[11\bar{2}]} = 58.3$
Diamond	45,47	442	528	$\sigma_{<111>} = 82.3$	$\tau_{(111)[11\bar{2}]} = 86.8$

Table 1. Voigt bulk modulus B_V, shear modulus G_V, and ideal strength (minimum tensile strength σ_{min} and shear strength τ_{min}) of transition metal tetraborides (TmB$_4$, Tm = Cr, Mn, Fe) calculated by first principles methods. Previous theoretical results for WB$_3$[6], MoB$_3$[6], OsB$_2$[44], ReB$_2$[12], B$_6$O[45], BN[46] and Diamond[45,47] are included for comparison. * is calculated using Voigt-Reuss-Hill approximation.

the relatively high ratio of $G/B \approx 0.957$ for $oP10[58]$-CrB$_4$, 0.879 for $oP10[58]$-MnB$_4$, 0.674 for $oP10[58]$-FeB$_4$, we conclude that all these tetraborides are brittle[49,51]. Even in brittle solids, a brittle to ductile transition is possible at an elevated temperature where the nucleation of dislocation embryos becomes possible prior to cleavage propagation[50].

It is known that high elastic moduli do not guarantee high resistance against plastic deformation because upon finite shear electronic instabilities and transformations to softer phases with lower shear resistance often occur[9,26]. The anisotropic ideal shear strength of $oP10[58]$-TmB$_4$ may be obtained from the calculated stress-strain relationships along different crystallographic planes and directions. The slip systems of (110)[1–10] and (010)[101] were reported as the weakest ones for $oP10[58]$-CrB$_4$ by Li *et al.*[23] and by Niu *et al.*[19], respectively. A similar disagreement exists also for the weakest slip system in FeB$_4$, where (110)[001] has been reported by Li *et al.*[28] but (111)[11–2] by Zhang *et al.*[48]. We studied all the four slip systems in more detail. Our results suggest that the (110)[1–10] slip systems is the weakest one for CrB$_4$, whereas (110)[001] is the weakest for FeB$_4$ and MnB$_4$. Figure 4a–c show the calculated dependence of the stress, magnetic moment and total energy on strain for $oP10[58]$-CrB$_4$, $oP10[58]$- MnB$_4$ and $oP10[58]$- FeB$_4$ along their weakest slip systems. The minimum strength for the three TmB$_4$ is shown in Table 1 and compared with previous results for these tetraborides[19,23,27,28,30–32], and with those of WB$_3$ and MoB$_3$[6], ReB$_2$[12], OsB$_2$[44], B$_6$O[45], c-BN[46] and diamond[45,47]. It is seen that the minimum shear strengths of $oP10[58]$-CrB$_4$ of 36.2 GPa in the (110)[1–10] slip system are comparable to those of WB$_3$ (37.7 GPa) and ReB$_2$ (34.4 GPa), but they are much lower than those of c-BN (58.3 GPa[46]). This suggests that CrB$_4$ cannot be intrinsically stronger than WB$_3$ in view of the fact that its strength is between that of WB$_3$ and ReB$_2$. These results are in agreement with the recent experiments in which the load-invariant ("asymptotic") Vickers hardness of CrB$_4$ (23.3 GPa[21] and 28.6 GPa[22]) was found to be comparable to that of ReB$_2$. The high hardness of 48 GPa for CrB$_4$ "predicted" by Niu *et al.*[19] on the basis of the "hardness model" is not justified. Similar conclusions apply also for MnB$_4$ and FeB$_4$ because a much lower ideal shear strength is found for $oP10[58]$-MnB$_4$ (35.1 GPa) and $oP10[58]$-FeB$_4$ (25.7 GPa), although Niu *et al.*[19] predicted a high value of hardness of 41.5 GPa for MnB$_4$. The reason is simply the fact that the "theoretical models of hardness" compares in fact elastic stiffness, and do not account for electronic instabilities upon a finite shear[18,26].

Bond deformation mechanism of $oP10[58]$-TmB$_4$. In view of the mechanical weakness of $oP10[58]$-TmB$_4$, we investigated the bond deformation paths and electronic instability mode of $oP10[58]$-TmB$_4$ along the weakest shear path. Figure 4a,c show that both stress-strain and total energy-strain curves are smooth, i.e. no distinct electronic instabilities occur as in the cases of ReB$_2$[18] and WB$_3$[6], but not for the change of magnetic moment for FeB$_4$. Figure 4d–f show the variation of the VCDD from the equilibrium ($\gamma = 0.0000$), to a shear strain $\gamma = 0.1717$ corresponding to the stress maximum and at shear strain $\gamma = 0.4002$ after the shear instability for CrB$_4$ in the weakest (110)[1–10] slip system. One can see the change of in-plane lengths of the B1–B2 and B3–B4 bonds with respect to (001) planes from ~1.85 Å at equilibrium to ~2.11 Å at maximum stress. With the elongation of B1–B2 and B3–B4 bond lengths, the magnitude of charge depletion between them increases gradually
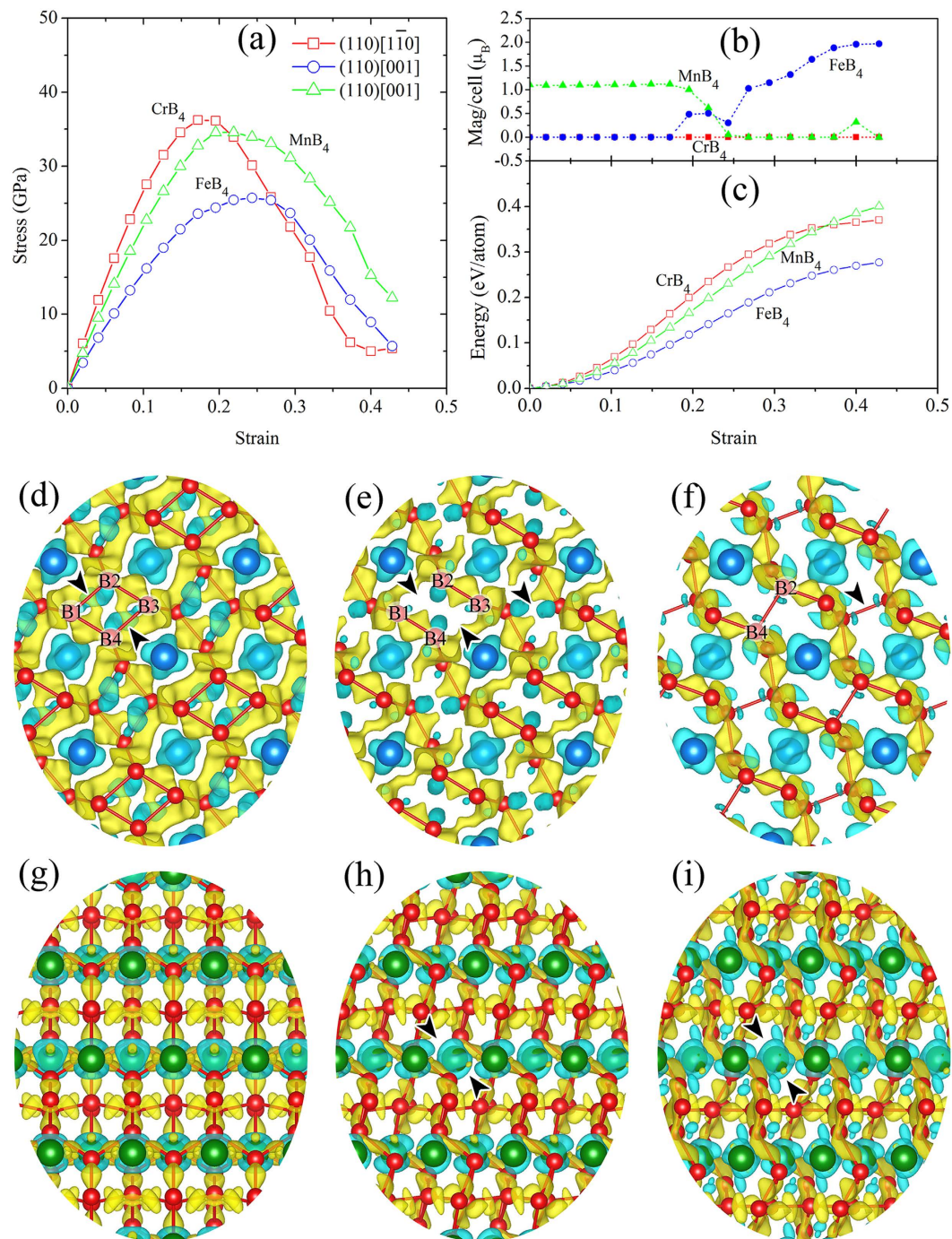
Figure 4. Analysis of shear deformations. (**a**) Stress-strain, (**b**) magnetic moment-strain and (**c**) energy-strain relationships for $oP10[58]$- CrB_4, $oP10[58]$- MnB_4 and $oP10[58]$- FeB_4 along the weakest shearing path. The deformation paths are indicated in the figures. The snapshots of deformed bond structure and VCDD viewed along crystallographic [001] direction, i.e. z axis in Cartesian coordinate system at shear strain of (**d**) $\gamma = 0.0000$, (**e**) $\gamma = 0.1717$ (at peak) and (**f**) $\gamma = 0.4002$ (after instability) for CrB_4 along the weakest (110)[1–10] slip system, and (**g**) $\gamma = 0.0000$, (**h**) $\gamma = 0.2434$ (at peak), and (**i**) $\gamma = 0.4002$ (after instability) for FeB_4 along the weakest (110)[001] slip system. The black arrows in (**d–i**) indicate the position of bond instability.

before the stress reaches the peak value of about 25.7 GPa (see Fig. 4e). After the peak stress, the B2 atom and B4 atom come closer together and form B2–B4 bonds with length of ~1.97 Å at a strain of 0.4002, while the B1 and B3 atoms further separate. The shear deformation after the peak stress is accompanied by a stress decrease to about 5 GPa (Fig. 4a).

In FeB_4 and MnB_4, the weakest link does not appear along the (110)[1–10] shear. Therefore we concentrate on the deformation within the (110)[001] slip system. In view of the similarity between FeB_4 and MnB_4, we shall take FeB_4 as an illustrative example. Figure 4g–i show the variation of the VCDD isosurfaces in equilibrium
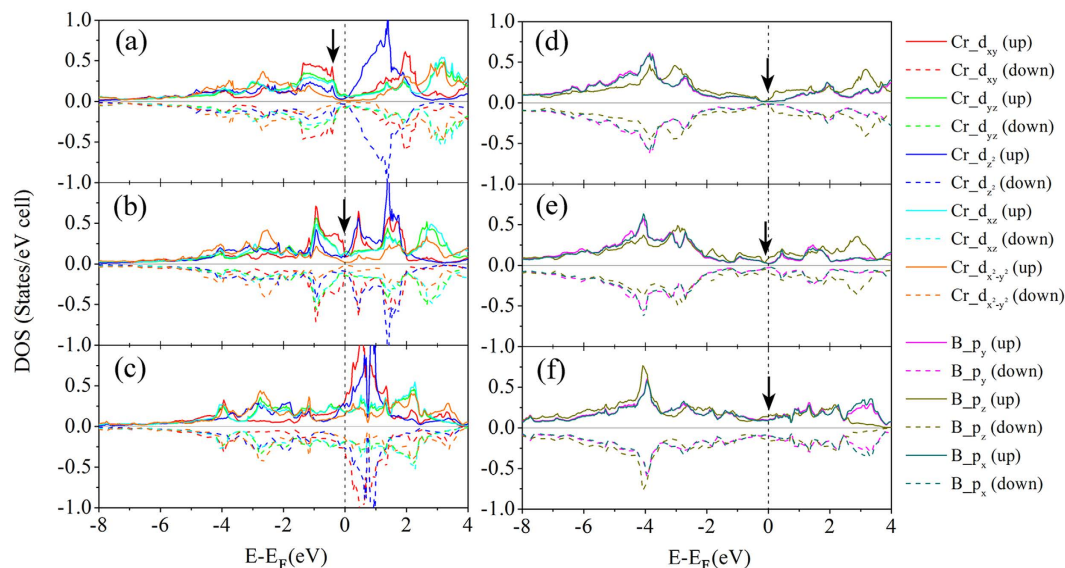
Figure 5. Orbital-decomposed electronic density of states of *oP*10[58]-CrB$_4$. (**a,d**) at equilibrium, (**b,e**) at a strain of 0.1717, (**c,f**) at a strain of 0.4002. The reference Cartesian coordinates was chosen such that the x axis is normal to crystallographic (1–10) plane, the y axis is along the crystallographic [110] direction and the z axis along the [001] direction respectively. The black arrows in (**a–c**) indicate the change of d$_{xy}$ state, and those in (**d–f**) show the change of pseudogap at Fermi level.

($\gamma = 0.0000$), at a shear strain of $\gamma = 0.2434$ corresponding to the maximum stress, and at $\gamma = 0.4002$ after the shear instability of FeB$_4$, respectively. No significant bond weakening or breaking appear before the shear stress reaches the maximum value at strain of about 0.25. After the shear instability, a multiple out-of-plane bond weakening and breaking appears between the {001} planes (see the regions marked by black arrows in Fig. 4h,i). In the following orbital analysis we shall show that such bond weakening is attributed to the electronic instability between the d orbitals of Fe and p orbitals of B, which are responsible for the out-of-plane bonding between {001} planes.

Electronic origin of lattice instability under shearing. For that purpose, we analyze the change of orbital-decomposed DOS of d orbitals of Tm and p orbitals of boron in TmB$_4$ before and after lattice instability. Figure 5a–f shows the orbital-decomposed DOS of CrB$_4$ at equilibrium, at a strain of 0.1717, and at a strain of 0.4002. Upon shear but before the lattice instability, the occupied d$_{xy}$ states located below E_F move towards E_F (see the red curve between -2 eV and 0 eV in Fig. 5a,b), while the peak of d$_{xy}$ above E_F move downwards and split into two parts between 0 and 1 eV, and between 1 and 2 eV. The splitting feature is also observed for the d$_z$^{2} states above E_F (see blue curve between 0 eV and 2 eV in Fig. 5a,b). During this process, the shape of the other three d-states around E_F does not change significantly. After the lattice instability (see Fig. 5c), most of the d$_{xy}$ and d$_z$^{2} states between -2 eV and 0 eV have vanished, and both contribute substantially to peaks in the DOS between 0 and 2 eV above E_F. At the same time, the pseudogap in the p$_z$ states of boron became narrower and finally vanished, while p$_x$ and p$_y$ increase their contribution at E_F after the lattice instability. At the peak stress, all three p orbitals contribute to the states at E_F. Therefore, the change of the DOS arising from the d$_{xy}$ orbitals of Cr and from p$_x$ and p$_y$ orbitals of B are mainly responsible for the in-plane bond weakening of B1–B2 and B3–B4 bonds within the x–y plane, as shown above.

Figure 6 shows the orbital-decomposed EDOS of the (110)[001] slip system of FeB$_4$ in equilibrium, at a strain of 0.2434 corresponding to the stress maximum, and at strain 0.4002 after the shear instability. In equilibrium, dz^2 states show a pseudogap at E_F whereas the other four d orbitals contribute mostly to the finite value at E_F. Before the instability, the peaks of all five orbitals between -6 eV and 0 eV move towards E_F, and at the maximum stress one profound peak of d$_z$^{2} character is seen at the Fermi level giving large contribution to the states at E_F, while nearly all peaks of other spin-up orbitals above the Fermi level vanish. After the lattice instability, the states of all spin-down orbitals move further upwards, whereas the d$_{xz}$ spin-down states appear above Fermi level. The appearance of boron p$_z$ states at the Fermi level and the decrease of peaks of p$_x$ and p$_y$ states can be clearly seen in Fig. 6d–f. Therefore we can conclude that the electronic instability of FeB$_4$ during (110)[001] shear is mainly due to the changes of the energies of states of Fe d$_z$^{2} and d$_{xz}$ orbitals, and of p$_z$ orbitals of B. MnB$_4$ shows a similar instability as FeB$_4$, therefore we do not discuss it here in any further detail (see Fig. S8 in supplemental materials).

The electronic instability of TmB$_4$ (Tm = Cr, Mn and Fe) upon shear due to d orbitals of Tm and p orbitals of B does not resemble the cases of ReB$_2$[18] and WB$_3$[6]. The important difference is that in TmB$_4$ the covalent bond networks are mainly responsible for the shear instability, while metal-boron or metal-metal bonds are the carrier of the shear instability in ReB$_2$ and WB$_2$. Although the three dimensional covalent network has been proposed to be responsible for high hardness in transition metal borides for a long time, our results show uniquely that the 3D boron network in the tetraborides may not be strong enough to provide these materials with high plastic
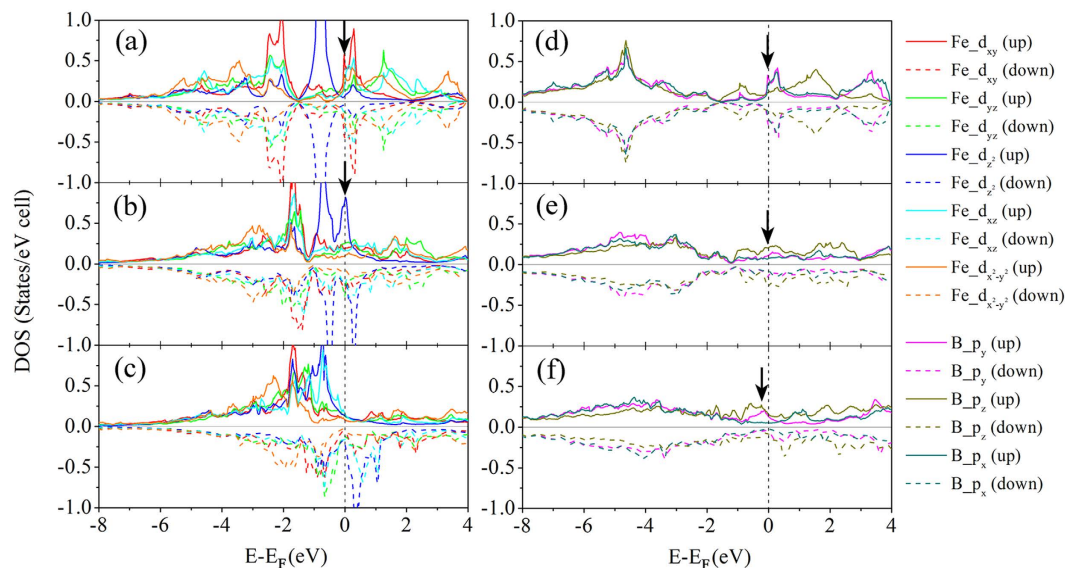
Figure 6. Orbital-decomposed electronic density of states of *oP*10[58]-FeB$_4$. (**a**,**d**) at equilibrium, (**b**,**e**) at a strain of 0.2434, (**c**,**f**) at a strain of 0.4002. The reference Cartesian coordinate was chosen such that the x axis is normal to crystallographic (1–10) plane, the y axis is along the crystallographic [110] direction and the z axis along [001] direction respectively. The black arrows in Fig. (**a**–**c**) indicate that the major contributions at Fermi level changes from d$_{xy}$ to d$_z{}^2$ state during shear, while arrows shown in Fig. (**d**–**f**) show the change of p$_z$ state at Fermi level.

resistance. Because the strength of a real crystalline material is limited by a variety of defects, such as dislocations, cracks, grain boundaries and others, it is usually orders of magnitude smaller than that of an ideal crystal. The Peierls–Nabarro (PN) stress of dislocations provides a realistic explanation on plastic resistance of a real crystal and can be correlated to shear moduli and ideal shear strength[53–55] as $\tau_p = K \exp(-\alpha\zeta/b)$, where $\alpha = 2\pi$ and $K = G/(1-\nu)$ for edge dislocation and $K = G$ for screw dislocation, b is the Burgers vector, ν is the Poisson ratio, and ζ is the dislocation half-width which can be expressed as $\zeta = Kb/4\pi\tau_{max}$, where τ_{max} is the ideal shear strength. Thus, the plastic resistance of a crystal depends mainly on the shear modulus, ideal shear strengths, lattice topology, bonding nature and deformation mode. The present work emphasizes the necessity to conduct a combinational analysis of the lattice stability, of the values of shear moduli, of the anisotropic shear strength, of the complexity of lattice topology and its changes during shear, of the nature of chemical bonding, and others which are critical parameters in Peierls–Nabarro dislocation model of plastic lattice resistance[53–55]. Despite a century of research on dislocation mediated plasticity, a systematic connection to those quantities derived from first principle calculations has not been rationalized, inducing massive applications of a single parameter e.g. elastic moduli or ideal shear strength, to directly quantify the mechanical strength and hardness of a real material[3,4,9–12,19,23,24,28].

Discussion

In summary, we carried out comprehensive density functional theory calculations to determine the thermodynamic, mechanical and phonon stabilities, the deformation paths and the electronic instability modes of orthorhombic TmB$_4$. The electronic structure calculations reveal that the transformation from *oI*10[71]-TmB$_4$ to *oP*10[58]-TmB$_4$ can be explained by the variation of the in-plane electronic structure within (001) planes and the formation of new boron-boron bonds at hollow sites by distortion of boron networks. These processes significantly enhance the electronic hybridization of d orbitals of Tm with p orbitals of B by crystal field splitting. Depending on the different deformation paths (slip systems), different orbitals are responsible for the electronic instability upon finite shear. The relatively low shear moduli and ideal strengths of TmB$_4$ suggest that these materials cannot be intrinsically superhard. The instability of weak 3D boron covalent networks is found to be responsible for the weakness of *oP*10[58]-TmB$_4$. These results illustrate the importance and necessity of a combinational analysis of a variety of parameters related to plastic deformation of the crystalline materials, and their combination in the attempt to design new intrinsically hard and superhard materials.

Methods

First principles calculations. The present first-principles density functional theory (DFT) calculations of the formation energy of TmB$_4$, Tm = Cr, Mn and Fe were done by means of the VASP code[35] with the projector augmented wave method[36] employed to describe the electron-ion interaction and the generalized-gradient approximation of Perdew-Burke-Ernzerhof (PBE)[56] for the exchange correlation term. The integration in the Brillouin zone has been done on special k grids for the phases that were under consideration, which were determined according to the Monkhorst-Pack scheme, the energy cutoff of 600 eV, and the tetrahedron method with Blöchl corrections for the density of states and smearing methods for the stress calculations. The verification of

the reliability of our calculations has been done by calculating the total energies, equilibrium lattice parameter, and bulk modulus of TmB_4 and compared with previous theoretical and experimental values in the present work, and of a number of other materials in our earlier work. In the present studies, all DFT calculations are performed with spin-polarized scheme because of the appearance of magnetic momentum during the deformation. Nevertheless, in cases where no magnetic momentum has been found, additional non-spin-polarized calculation is used to check its possible influence.

The phonon dispersion. The phonon calculations were performed within the harmonic approximation using the direct method[57] based on the calculated non-vanishing Hellman-Feynman forces employing the Phonopy code[58]. To confirm our results, we also used a linear response method based on the perturbation theory as implemented in VASP code.

The elastic constants. For orthorhombic crystals (Group numbers 16–74), there are nine independent elastic constants usually referred to as c_{11}, c_{22}, c_{33}, c_{44}, c_{55}, c_{66}, c_{12}, c_{13}, and c_{23}. In the following, we give a set of simple strain configurations and the corresponding strain-energy density variations $\Delta E/V_0$. (r1) $\varepsilon = (\delta,0,0,0,0,0)$ with relation $\Delta E/V_0 = \tau_1\delta + \frac{1}{2}C_{11}\delta^2$, (r2) $\varepsilon = (0,\delta,0,0,0,0)$ with relation $\Delta E/V_0 = \tau_2\delta + \frac{1}{2}C_{22}\delta^2$, (r3) $\varepsilon = (0,0,\delta,0,0,0)$ with relation $\Delta E/V_0 = \tau_3\delta + \frac{1}{2}C_{33}\delta^2$, (r4) $\varepsilon = (0,0,0,\delta,0,0)$ with relation $\Delta E/V_0 = \tau_4\delta + \frac{1}{2}C_{44}\delta^2$, (r5) $\varepsilon = (0,0,0,0,\delta,0)$ with relation $\Delta E/V_0 = \tau_5\delta + \frac{1}{2}C_{55}\delta^2$, (r6) $\varepsilon = (0,0,0,0,0,\delta)$ with relation $\Delta E/V_0 = \tau_6\delta + \frac{1}{2}C_{66}\delta^2$, (r7) $\varepsilon = (\delta,\delta,0,0,0,0)$ with relation $\Delta E/V_0 = (\tau_1 + \tau_2)\delta + \frac{1}{2}(C_{11} + C_{22} + 2C_{12})\delta^2$, (r8) $\varepsilon = (\delta,0,\delta,0,0,0)$ with relation $\Delta E/V_0 = (\tau_1 + \tau_3)\delta + \frac{1}{2}(C_{11} + C_{33} + 2C_{13})\delta^2$, (r9) $\varepsilon = (0,\delta,\delta,0,0,0)$ with relation $\Delta E/V_0 = (\tau_2 + \tau_3)\delta + \frac{1}{2}(C_{22} + C_{33} + 2C_{23})\delta^2$.

The stress-strain relationships. First, the atomic basis vectors of a given crystal cell were projected onto the Cartesian coordinates R with one axis vector being parallel to the imposed strain direction for the tension. For the shear, one axis vector was perpendicular to the slip plane and another one was parallel to the slip direction in that plane. Afterwards, the crystal has been incrementally deformed by transforming the unstrained atomic basis vector matrices R to the strained ones R' using the deformation matrices.

$$R' = R \cdot \begin{pmatrix} 1 + e_1 & e_6/2 & e_5/2 \\ e_6/2 & 1 + e_2 & e_4/2 \\ e_5/2 & e_4/2 & 1 + e_3 \end{pmatrix} \tag{1}$$

where $e_1 = e_{xx}$, $e_2 = e_{yy}$, $e_3 = e_{zz}$, $e_4 = e_{zy} + e_{yz}$, $e_5 = e_{zx} + e_{xz}$, and $e_6 = e_{yx} + e_{xy}$ are the strain components in the Voigt notation. The diagonal strain components e_{xx}, e_{yy}, and e_{zz} represent the tension while the off-diagonal components represent the shear. In order to keep the crystal under a stress state of uniaxial tension or shear, the strained cell has been relaxed for both the atomic basis vectors and for the atom coordinates inside the unit cell by keeping the applied strain component fixed and relaxing the other five strain components until their conjugate stress components i.e., Hellmann–Feynman stresses reached negligible values. Such a relaxation scheme is accomplished by using a slightly modified VASP code with specific constraints of strain components. To ensure that the strain path is continuous, the starting position at each strain step has been taken from the relaxed coordinates of the previous strain step. In the instance of having a large strain, the crystal symmetry may be changed and the Brillouin zone significantly deformed. Therefore we adopt a high energy cutoff of 600 eV and verified the convergence of the calculations of the stress-strain curves by using different meshes of k points. Although the spin-polarized calculation does not have big impact on the shear strength on FeB_4 and CrB_4, we performed the spin-polarized calculations for a comparison because of the significant magnetic effect on the results of MnB_4 and possible appearance of magnetic moment during severe deformation.

Evolutionary Structure Searches. Structure searches were performed using the open-source evolutionary algorithm (EA) XtalOpt[38,39] along with the default parameter set from ref. 38. EA runs were carried out on the TmB_4 with 2, 3 and 4 formula units in the primitive cell. In this algorithm a new offspring is procreated as soon as an individual is optimized and the parents are chosen from a population based pool. The population size were around 735, 225, 110 for the 2, 3 and 4 formula unit cells of CrB_4, respectively, and 200, 225, 160 for the 2, 3 and 4 formula unit cells of MnB_4, respectively. In each run the same low enthalpy structure was found at least 3 times (often more) before the run was terminated. A six-step structural-optimization scheme was used for all runs, and each step employed the geometry of the structure from the previous step for the initial geometry. Only the ions were allowed to relax in the first two steps, while the last four steps also allowed the lattice parameters to relax. The precision of the calculation was increased at each step. The calculations were performed using the PBE exchange-correlation functional, the PAW method and an energy cut-off of 450 eV in the final step. The lowest energy structures from each search were optimized using the aforementioned computational settings, to obtain a more accurate energy ranking.

References

1. Mohammadi, R. *et al.* an inexpensive superhard material. *P. Natl. Acad. Sci. USA* **108,** 10958–10962 (2011).
2. Mohammadi, R. *et al.* Toward inexpensive superhard materials: tungsten tetraboride-based solid solutions. *J. Am. Chem. Soc.* **134,** 20660–20668 (2012).
3. Gu, Q., Krauss, G. & Steurer, W. Transition Metal Borides: Superhard versus ultra-incompressible. *Adv. Mater.* **20,** 3620 (2008).
4. Levine, J. B., Tolbert, S. H. & Kaner, R. B. Advancements in the search for superhard ultra-incompressible metal borides. *Adv. Funct. Mater.* **19,** 3519–3533 (2009).

5. Li, Q., Zhou, D., Zheng, W. T., Ma, Y. M. & Chen, C. F. Global structural optimization of tungsten borides. *Phys. Rev. Lett.* **110,** 136403 (2013).

6. Zhang, R. F. *et al.* Stability and strength of transition-metal tetraborides and triborides. *Phys. Rev. Lett.* **108,** 255502 (2012).

7. Lech, A. T., Turner, C. L., Mohammadi, R., Tolbert, S. H. & Kaner, R. B. Structure of superhard tungsten tetraboride: A missing link between MB_2 and MB_{12} higher borides. *P. Natl. Acad. Sci. USA* **112,** 3223–3228 (2015).

8. Kotmool, K. *et al.* Revealing an unusual transparent phase of superhard iron tetraboride under high pressure. *P. Natl. Acad. Sci. USA* **111,** 17050–17053 (2014).

9. Veprek, S. Recent search for new superhard materials: Go nano! *J. Vac. Sci. Technol. A* **31,** 050822 (2013).

10. Cumberland, R. W. *et al.* Osmium diboride, an ultra-incompressible, hard material. *J. Am. Chem. Soc.* **127,** 7264–7265 (2005).

11. Chung, H. Y. *et al.* Synthesis of ultra-incompressible superhard rhenium diboride at ambient pressure. *Science* **316,** 436–439 (2007).

12. Zhang, R. F., Veprek, S. & Argon, A. S. Mechanical and electronic properties of hard rhenium diboride of low elastic compressibility studied by first-principles calculation. *Appl. Phys. Lett.* **91,** 201914 (2007).

13. Wang, M., Li, Y. W., Cui, T., Ma, Y. M. & Zou, G. T. Origin of hardness in WB_4 and its implications for ReB_4, TaB_4, MoB_4, TcB_4, and OsB_4. *Appl. Phys. Lett.* **93,** 101905 (2008).

14. Liang, Y. C., Yuan, X. & Zhang, W. Q. Thermodynamic identification of tungsten borides. *Phys. Rev. B* **83,** 220102 (2011).

15. Zhang, M. G., Wang, H., Wang, H. B., Cui, T. & Ma, Y. M. Structural modifications and mechanical properties of molybdenum borides from first principles. *J. Phys. Chem. C* **114,** 6722–6725 (2010).

16. Cheng, X. *et al.* Interstitial-boron solution strengthened WB_{3+x}. *Appl. Phys. Lett.* **103,** 171903 (2013).

17. Tao, Q. *et al.* Exploring hardness and the distorted sp^2 hybridization of B-B Bonds in WB_3. *Chem. Mater.* **26,** 5297–5302 (2014).

18. Zhang, R. F., Legut, D., Niewa, R., Argon, A. S. & Veprek, S. Shear-induced structural transformation and plasticity in ultraincompressible ReB_2 limit its hardness. *Phys. Rev. B* **82,** 104104 (2010).

19. Niu, H. Y. *et al.* Structure, bonding, and possible superhardness of CrB_4. *Phys. Rev. B* **85,** 144116 (2012).

20. Niu, H. Y. *et al.* Variable-composition structural optimization and experimental verification of MnB_3 and MnB_4. *Phys. Chem. Chem. Phys.* **16,** 15866–15873 (2014).

21. Knappschneider, A. *et al.* Possible superhardness of CrB_4. *Inorg. Chem.* **52,** 540–542 (2013).

22. Wang, S. *et al.* Crystal structures, elastic properties, and hardness of high-pressure synthesized CrB_2 and CrB_4. *J. Superhard Mater.* **36,** 279–287 (2014).

23. Li, B., Sun, H., Zang, C. P. & Chen, C. F. Fundamental constraints on the strength of transition-metal borides: The case of CrB_4. *Phys. Rev. B* **87,** 174106 (2013).

24. Gou, H. Y. *et al.* Discovery of a superhard iron tetraboride superconductor. *Phys. Rev. Lett.* **111,** 157002 (2013).

25. Brazhkin, V. *et al.* What-does 'harder than diamond' mean? *Nat. Mater.* **3,** 576–577 (2004).

26. Veprek, S., Zhang, R. F., Veprek-Heijman, M. G. J., Sheng, S. H. & Argon, A. S. Superhard nanocomposites: Origin of hardness enhancement, properties and applications. *Surf. Coat. Tech.* **204,** 1898–1906 (2010).

27. Gou, Y. P., Fu, Z., Liang, Y. C., Zhong, Z. & Wang, S. M. Electronic structures and mechanical properties of iron borides from first principles. *Solid St. Comm.* **187,** 28–32 (2014).

28. Li, B., Sun, H. & Chen, C. F. First-principles calculation of the indentation strength of FeB_4. *Phys. Rev. B* **90,** 014106 (2014).

29. Wang, Q. Q. *et al.* Is orthorhombic iron tetraboride superhard? *J. Materiomics* **1,** 45–51 (2015).

30. Liang, Y. C., Yuan, X., Gao, Y. F., Zhang, W. Q. & Zhang, P. H. Phonon-assisted crossover from a nonmagnetic Peierls Insulator to a magnetic Stoner metal. *Phys. Rev. Lett.* **113,** 176401 (2014).

31. Yang, M. *et al.* Structural distortion and band gap opening of hard MnB_4 in comparison with CrB_4 and FeB_4. *J. Solid State Chem.* **213,** 52–56 (2014).

32. Zhang, X. Y. *et al.* First principle study of elastic and thermodynamic properties of FeB_4 under high pressure. *J. Appl. Phys.* **114,** 183517 (2013).

33. Kolmogorov, A. N. *et al.* New Superconducting and Semiconducting Fe-B Compounds Predicted with an Ab Initio Evolutionary Search. *Phys. Rev. Lett.* **105,** 217003 (2010).

34. ICSD-Inorganic Crystal Structure Database, http://www2.fiz-karlsruhe.de/icsd_home.html (Date of access: 08/07/2014).

35. Kresse, G. & Furthmüller, J. Efficiency of ab-initio total energy calculations for metals and semiconductors using a plane-wave basis set. *Comput. Mater. Sci.* **6,** 15–50 (1996).

36. Kresse, G. & Joubert, J. From ultrasoft pseudopotentials to the projector augmented-wave method. *Phys. Rev. B* **59,** 1758 (1999).

37. Van der Geest, A. G. & Kolmogorov, A. N. Stability of 41 metal-boron systems at 0 GPa and 30 GPa from first principles. *Calphad* **46,** 184–204 (2014).

38. Lonie, D. C. & Zurek, E. XTALOPT: An open-source evolutionary algorithm for crystal structure prediction. *Comput. Phys. Commun.* **182,** 372–387 (2011).

39. Lonie, D. C. & Zurek, E. XTALOPT version r7: An open-source evolutionary algorithm for crystal structure prediction. *Comput. Phys. Commun.* **182,** 2305–2306 (2011).

40. Bialon, A. F. *et al.* Possible routes for synthesis of new boron-rich Fe-B and $Fe_{1-x}Cr_xB_4$ compounds. *Appl. Phys. Lett.* **98,** 081901 (2011).

41. Burdett, J. K. & Canadell, E. Chromium boride (CrB_4) and manganese boride (MnB_4): electronic structures of two unusual systems containing the tetragonal carbon net. *Inorg. Chem.* **27,** 4437–4444 (1988).

42. Bader, R. F. W. In *Atoms in molecules-A quantum theory* 1 (Oxford University Press, 1990).

43. Wu, Z. J. *et al.* Crystal structures and elastic properties of superhard IrN_2 and IrN_3 from first principles. *Phys. Rev. B* **76,** 054115 (2007).

44. Zhang, R. F. *et al.* Bond deformation paths and electronic instabilities of ultraincompressible transition metal diborides: Case study of OsB_2 and IrB_2. *Phys. Rev. B* **90,** 094115 (2014).

45. Zhang, R. F., Lin, Z. J., Zhao, Y. S. & Veprek, S. Superhard materials with low elastic moduli: Three-dimensional covalent bonding as the origin of superhardness in B_6O. *Phys. Rev. B* **83,** 092101 (2011).

46. Zhang, R. F., Veprek, S. & Argon, A. S. Anisotropic ideal strengths and chemical bonding of wurtzite BN in comparison to zincblende BN. *Phys. Rev. B* **77,** 172103 (2008).

47. Zhang, R. F., Lin, Z. J. & Veprek, S. Anisotropic ideal strengths of superhard monoclinic and tetragonal carbon and their electronic origin. *Phys. Rev. B* **83,** 155452 (2011).

48. Zhang, M. *et al.* Hardness of FeB_4: Density functional theory investigation. *J. Chem. Phys.* **140,** 174505 (2014).

49. Rice, J. R., Beltz, G. E. & Sun, Y. In *Topics in fracture and fatigue* (ed. Argon, A. S.) 1–58 (Springer, 1992).

50. Xu, G., Argon, A. S. & Ortiz, M. Critical configurations for dislocation nucleation from crack tips. *Philos. Mag. A* **75,** 341–367 (1997).

51. Pugh, S. F. X. C. I. I. Relations between the elastic moduli and the plastic properties of polycrystalline pure metals. *Philos. Mag. A* **45,** 823–843 (1954).

52. Mattesini, M., Ahuja, R. & Johansson, B. Cubic Hf_3N_4 and Zr_3N_4: A class of hard materials. *Phys. Rev. B* **68,** 184108 (2003).

53. Zhang, R. F., Sheng, S. H. & Veprek, S. Origin of different plastic resistance of transition metal nitrides and carbides: Stiffer yet softer. *Scripta Mater.* **68,** 913–916 (2013).

54. Yu, X. H. *et al.* High pressure phase-transformation induced texture evolution and strengthening in zirconium metal: experiment and modeling. *Sci. Rep.* **5,** 12552 (2015).

55. Argon A. S. In *Strengthening mechanisms in crystal plasticity* 78 (Oxford University Press, 2008).
56. Perdew, J. P., Burke, K. & Ernzerhof, M. Generalized gradient approximation made simple. *Phys. Rev. Lett.* **77,** 3865 (1996).
57. Parlinski, K., Li, Z. Q. & Kawazoe, Y. First-principles determination of the soft mode in cubic ZrO_2. *Phys. Rev. Lett.* **78,** 4063 (1997).
58. Togo, A., Oba, F. & Tanaka, I. First-principles calculations of the ferroelastic transition between rutile-type and $CaCl_2$-type SiO_2 at high pressures. *Phys. Rev. B* **78,** 134106 (2008).

Acknowledgements

Author Contributions

R.F.Z., X.D.W., D.L. and Z.H.F. participate in the first principles calculations. All authors contributed the idea and participated in the scientific discussions, manuscript comments and corrections.

Additional Information

Supplementary information accompanies this paper at http://www.nature.com/srep

Competing financial interests: The authors declare no competing financial interests.

How to cite this article: Zhang, R. F. *et al.* Crystal Field Splitting is Limiting the Stability and Strength of Ultra-incompressible Orthorhombic Transition Metal Tetraborides. *Sci. Rep.* **6**, 23088; doi: 10.1038/srep23088 (2016).